

Direct imaging discovery of a young giant planet orbiting on solar system scales

T. Stolker¹, M. Samland², L. B. F. M. Waters⁵, M. E. van den Ancker⁶, W. O. Balmer^{3,4}, S. Lacour^{7,6}, M. L. Sitko¹¹, J. J. Wang⁸, M. Nowak⁹, A.-L. Maire¹⁰, J. Kammerer⁶, G. P. P. L. Otten³³, R. Abuter⁶, A. Amorim^{15,16}, M. Benisty², J.-P. Berger¹⁰, H. Beust¹⁰, S. Blunt⁸, A. Boccaletti⁷, M. Bonnefoy¹⁰, H. Bonnet⁶, M. S. Bordini¹⁷, G. Bourdarot¹⁷, W. Brandner², F. Cantalloube¹⁰, P. Caselli¹⁷, B. Charnay⁷, G. Chauvin¹⁸, A. Chavez⁸, A. Chomez^{7,10}, E. Choquet¹⁹, V. Christiaens²⁰, Y. Clénet⁷, V. Coudé du Foresto⁷, A. Cridland¹, R. Davies¹⁷, R. Dembet⁷, J. Dexter¹¹, C. Dominik¹², A. Drescher¹⁷, G. Duvert¹⁰, A. Eckart^{21,22}, F. Eisenhauer¹⁷, N. M. Förster Schreiber¹⁷, P. Garcia^{16,23}, R. Garcia Lopez^{24,2}, T. Gardner²⁵, E. Gendron⁷, R. Genzel^{17,26}, S. Gillessen¹⁷, J. H. Girard⁴, S. Grant¹⁷, X. Haubois²⁷, G. Heißel^{28,7}, Th. Henning², S. Hinkley²⁹, S. Hippler², M. Houllé¹⁸, Z. Hubert¹⁰, L. Jocou¹⁰, M. Keppler², P. Kervella⁷, L. Kreidberg², N. T. Kurtovic¹⁷, A.-M. Lagrange^{10,7}, V. Lapeyrère⁷, J.-B. Le Bouquin¹⁰, D. Lutz¹⁷, F. Mang¹⁷, G.-D. Marleau^{30,31,2}, A. Mérand⁶, M. Min¹³, P. Mollière², J. D. Monnier³², C. Mordasini³¹, D. Mouillet¹⁰, E. Nasedkin², T. Ott¹⁷, C. Paladini²⁷, T. Paumard⁷, K. Perraut¹⁰, G. Perrin⁷, O. Pfuhl⁶, N. Pourré¹⁰, L. Pueyo⁴, S. P. Quanz¹⁴, D. C. Ribeiro¹⁷, E. Rickman³⁴, Z. Rustamkulov³⁵, J. Shangguan³⁸, T. Shimizu¹⁷, D. Sing^{3,35}, J. Stadler^{36,37}, O. Straub³⁷, C. Straubmeier²¹, E. Sturm¹⁷, L. J. Tacconi¹⁷, E.F. van Dishoeck^{1,17}, A. Vigan¹⁹, F. Vincent⁷, S. D. von Fellenberg²², F. Widmann¹⁷, T. O. Winterhalder⁶, J. Woillez⁶, and S. Yazici¹⁷

(Affiliations can be found after the references)

Received ?; accepted ?

ABSTRACT

Context. HD 135344 AB is a young visual binary system that is best known for the protoplanetary disk around the secondary star. The circumstellar environment of the A0-type primary star, on the other hand, is already been depleted. HD 135344 A is therefore an ideal target to explore for recently formed giant planets without the obscuring effect of dust.

Aims. We search for and characterize substellar companions at HD 135344 A down to separations of about 10 au.

Methods. We observed HD 135344 A with VLT/SPHERE in the $H23$ and $K12$ bands, and obtained YJ and YJH spectroscopy. In addition, we carried out VLTI/GRAVITY observations for further astrometric and spectroscopic confirmation of a detected companion.

Results. We discovered a close-in, young giant planet, HD 135344 Ab, with a mass of about $10 M_J$. The multi-epoch astrometry confirms the bound nature, both by common parallax and common proper motion, thereby firmly ruling out the scenario of a non-stationary background star. The planet's orbit has a semi-major axis of approximately 15–20 au and its photometry is consistent with a mid L-type object. The inferred atmospheric and bulk parameters further confirm the young and planetary nature of the companion.

Conclusions. HD 135344 Ab is one of the youngest directly imaged planets that has fully formed and orbits on solar system scales. It will be valuable target for studying the early evolution and atmosphere of a giant planet that could have formed in the vicinity of the snowline.

Key words. Stars: individual: HD 135344 A, Planets and satellites: detection – Planets and satellites: gaseous planets – Techniques: high angular resolution

1. Introduction

HD 135344 AB is a visual binary system that is located in Upper Centaurus Lupus (UCL) region of the Sco-Cen OB association. The secondary F4-type star, HD 135344 B, has been studied for several decades because of its prominent IR excess. During more recent years, the protoplanetary disk has been spatially resolved, revealing a central cavity (Brown et al. 2009; Garufi et al. 2013), spiral arms (Muto et al. 2012), and variable shadowing by the inner disk (Stolker et al. 2017). Such disk features may point to planet-disk interactions, but the suspected planets have remained hidden (e.g., Maire et al. 2017; Cugno et al. 2024).

While planet formation appears to be ongoing at HD 135344 B, the circumstellar environment of the A0-type primary star, HD 135344 A, is already largely depleted given the absence of strong IR excess in the spectral energy distribution (SED). HD 135344 A and B are proper-motion

binary partners (Mason et al. 2001) with an angular separation of $21''.2$ (≈ 2800 au), so their circumstellar disks have likely evolved independently, depending on the eccentricity of the orbits. We note that the secondary star has been incorrectly referred to as HD 135344 in some cases, although the issue had already been pointed out by Coulson & Walther (1995).

The two stars in the HD 135344 AB binary system are expected to be coeval. The pre-main-sequence age of the secondary star can therefore be adopted as the age of the main-sequence primary star. Garufi et al. (2018) inferred an age of $11.9^{+3.7}_{-5.8}$ Myr for HD 135344 B by using stellar evolutionary tracks and the Gaia parallax. Apart from its age, giant planets on wide orbits are most commonly detected around intermediate-mass stars (e.g., Nielsen et al. 2019; Vigan et al. 2021). The youth, spectral type, and dust depleted environment make HD 135344 A therefore an excellent target to search for young giant planets.

Table 1: Observation details.

| UT date ^a | Instrument | Mode | DIT/NDIT/NEXP ^b | Airmass | Seeing ^c (arcsec) | τ_0 ^d (ms) | π ^e (deg) |
|----------------------|------------|------------|----------------------------|-----------|---------------------------------|-------------------------------|-----------------------------|
| 2019 May 09 | SPHERE | IRDIFS | 48/3/16 | 1.02–1.03 | 0.78±0.09 | 2.7 ± 0.3 | 43.8 |
| 2019 Jul 06 | SPHERE | IRDIFS | 48/3/16 | 1.02–1.03 | 0.66±0.10 | 5.3 ± 0.6 | 43.3 |
| 2021 Jul 16 | SPHERE | IRDIFS | 4/32/25 | 1.02–1.05 | 0.64±0.11 | 3.3 ± 0.5 | 78.3 |
| 2022 May 04 | SPHERE | IRDIFS_EXT | 4/32/24 | 1.02–1.05 | 0.84±0.18 | 4.5 ± 1.0 | 78.4 |
| 2022 Jul 19 | GRAVITY | ON-AXIS | 100/4/8 | 1.03–1.13 | 1.26±0.19 | 1.8 ± 0.2 | 46.0 |
| 2023 May 08 | GRAVITY | ON-AXIS | 100/4/7 | 1.03–1.13 | 0.95±0.09 | 3.6 ± 0.5 | 35.2 |
| 2023 Jul 01 | GRAVITY | ON-AXIS | 100/4/4 | 1.08–1.17 | 0.79±0.12 | 6.4 ± 5.2 | 12.2 |

Notes. ^(a) UT date at the start of the observations. ^(b) Detector integration time, number of integrations per exposure, and number of exposures. The listed values of the SPHERE observations are from IRDIS. ^(c,d) Sample mean and standard deviation of the DIMM seeing and coherence time. ^(e) Rotation by the parallactic angle.

In this work, we report on high-contrast imaging observations to explore for the first time the circumstellar environment of HD 135344 A. We discovered a young giant planet that we confirmed through a detailed astrometric and spectral analysis. The evidence for the bound and planetary nature accumulates along the presented observations and results. For simplicity, we will refer to the discovered source as HD 135344 Ab from here on.

2. Observations and data reduction

2.1. VLT/SPHERE high-contrast imaging

HD 135344 A was observed with VLT/SPHERE (Beuzit et al. 2019) on the nights of the 8th of May 2019, 5th of July 2019, 16th of July 2021, and 3rd of May 2022. The first observations were carried out with the IRDIFS mode, to benefit from the highest angular resolution. We used the IRDIS dual-band camera with the $H23$ filters (Dohlen et al. 2008; Vigan et al. 2010) and we obtained a low-resolution YJ spectrum ($R \approx 50$) with IFS (Claudi et al. 2008). The first observation, that led to the discovery, did not fully meet the requested conditions (hence it was repeated in July), but the quality was sufficient to get a robust detection. We then repeated the observation in 2021, to confirm the source at the same wavelength. In 2022, we used the IRDIFS_EXT mode, to obtain $K12$ dual-band imaging and a low-resolution YJH spectrum ($R \approx 30$).

Integration times and observing conditions are listed in Table 1. We used deep exposures with a detector integration time (DIT) of 48 and 64 seconds for the simultaneous IRDIS and IFS measurements, respectively, in 2019. After the detection of the source at a small separation, we decided to change the observing strategy. Specifically, we used a DIT of 4 and 6 seconds for IRDIS and IFS, respectively, to sample the speckle variation on a faster timescale, which is beneficial for the post-processing. We also left the satellite spots on throughout the observations, to enable a more accurate centering and flux calibration.

The IRDIS and IFS data were reduced with `vlt-sphere` (Vigan 2020)¹, which provides a Python wrapper for the EsoRex recipes. It also applies a recalibration of the IFS wavelength solution and it centers the coronagraphic frames based on the satellite spots. The post-processing of the IRDIS data was done with `PynPoint`², applying full-frame principal component anal-

ysis (PCA) for the subtraction of the stellar halo and speckles (Amara & Quanz 2012; Stolker et al. 2019). For the astrometric and photometric measurement, we followed the procedure outlined in Stolker et al. (2020), which corrects for self-subtraction and includes the systematic uncertainty in the error budget. The extracted fluxes have been corrected for the coronagraph throughput, which ranged from 97% to 93% as the separation of the planet decreased.

The post-processing of the IFS data was done with `TRAP`³, which is in particular a more powerful detection and calibration technique for sources at small separation since systematics are modeled in the temporal instead of spatial domain (Samland et al. 2021). We have analyzed the YJ and YJH spectra from 2021 and 2022, respectively, because these datasets were obtained with the continuous satellite spots. Similar to the IRDIS data, the amplitudes of the spots were used for identifying low quality frames and their temporal variation was accounted for in the spectral extraction. The wavelength-averaged S/N of the discovered source is 2.9 and 1.5 for the YJ and YJH spectra, respectively. The higher S/N of the YJ spectrum might be due to the better seeing conditions.

Contrasts were converted to magnitudes and fluxes by using a synthetic stellar spectrum and a flux-calibrated spectrum of Vega (Bohlin et al. 2014). Table A.1 in Appendix A lists the inferred stellar parameters and the synthetic magnitudes of HD 135344 A in the IRDIS filters that were computed from the posterior distributions. The synthetic IFS spectrum of HD 135344 A was extracted by sampling random spectra from the posterior, smoothing those to $R = 30$, and rebinning to the wavelength solution of the instrument.

2.2. VLT/GRAVITY dual-field interferometry

The system was also observed with the four Unit Telescopes (UTs) of VLT/GRAVITY on the nights of the 19th of July 2022, 8th of May 2023, and 1st of July 2023 (see Table 1). GRAVITY provides exquisite astrometric precision for directly imaged planets and medium-resolution ($R \approx 500$) K -band spectroscopy (GRAVITY Collaboration et al. 2017). We used the dual-field on-axis mode with the fringe-tracking fiber centered on the star and the science fiber alternating between the star and planet. This strategy enables referencing and accurate calibration of the interferometric visibilities (GRAVITY Collaboration et al. 2020;

¹ <https://github.com/avigan/SPHERE>

² <https://github.com/PynPoint/PynPoint>

³ <https://github.com/m-samland/trap>

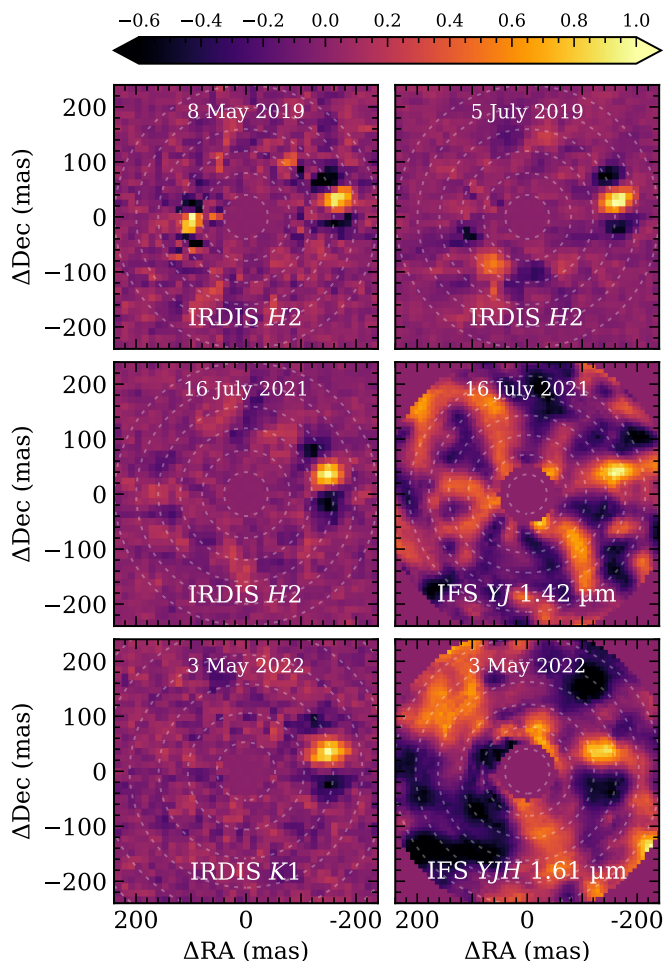


Fig. 1: Detections of HD 135344 Ab with VLT/SPHERE. For IRDIS, the images show the residuals from the PSF subtraction for one of the dual-band filters. For IFS, the images show the detection maps for one of the wavelength channels. The planet is seen in westward direction (i.e., towards the right). The color scale is linear and normalized to the brightest pixel in each image. The dotted circles indicate the separation from the central star in integer multiples of λ/D . The night of the observation is given in each panel.

Lacour et al. 2020). For the third observation (2023 Jul), we benefited from the recently commissioned faint mode, which turns off the metrology lasers during the science exposures, yielding a higher S/N detection of faint companions (Widmann et al. 2022).

Standard data reduction procedures were applied with the `run_gravi_reduce` script⁴ that calls the EsoRex recipes. We then used the `exoGravity`⁵ pipeline for phase referencing, subtracting the stellar component from the visibilities, and extracting the astrometry and spectrum (GRAVITY Collaboration et al. 2019, 2020; Nowak et al. 2020). After calibrating the full datasets, we excluded the baselines of UT3 from the 2023 May data, because of an issue with the metrology. The spectra of the discovered source have a wavelength-averaged S/N of 1.1, 2.6, and 5.0 (in chronological order). We only include the GRAVITY spectrum from 2023 July in the analysis, since a covariance-

weighted combination with the other two spectra did not improve the S/N, in particular because of stronger systematics in those two spectra. Similar to the IFS flux calibration, we used a synthetic spectrum to convert the contrast spectrum to fluxes, while taking into account the uncertainties on the stellar spectrum.

3. Results

3.1. Direct detection of a young giant planet

The residuals of the PSF subtraction from the imaging observations with SPHERE are shown in Fig. 1. We detected in 2019 an off-axis point source, HD 135344 Ab, in westward direction from the star, at an approximate separation of $4\lambda/D$ in H23. In 2021, the source was again detected, but at a somewhat smaller separation, and in 2022 also with the K12 filters. The PSF shape is typical for a post-processed point source. The negative lobes are due to the inherent self-subtraction effect by angular differential imaging (ADI). The source clearly stands out against the fainter speckle field in the background and is detected with $S/N \approx 10$ in all IRDIS imaging data. We did not detect extended emission in the data, so the circumstellar environment appears indeed depleted in small dust. There is also a feature seen in the IRDIS image from 2019 May in eastward direction, at a separation of $2.5\lambda/D$ from the star. It appears noisier compared to HD 135344 Ab and does more quickly self-subtract with an increasing number of components. Two months later, it was not detected so it is likely a speckle residual, since neither a background star nor a planet could have moved sufficiently to be hidden behind the coronagraph.

The SPHERE data were not fully conclusive with confirming that the discovered source was bound to HD 135344 A, hence we decided to follow up with the GRAVITY instrument. Figure 2 shows the detection maps of the GRAVITY observations. There is a clear detection of the planet in all datasets. We adopted the feature with the highest $\Delta\chi^2$ as the position of the planet, at which also the contrast spectrum was extracted. The pattern and elongated shapes in the detection maps depend on the coverage of the (u, v) -plane (i.e., UT baselines and field rotation). For the observation in 2022, the pointing of the fiber was 13.5 mas south from the actual location of the planet, resulting in a fiber coupling efficiency of 0.89. For the other two observations, the fiber position was (almost) spot-on with the planet due to the improved orbital constrained.

3.2. Relative astrometry: planet or background star?

HD 135344 AB is located in the Sco-Cen OB association, which is close to the direction of the Galactic center. Typically, there are multiple, if not many, background sources in the $12'' \times 12''$ field of view of the IRDIS camera. Indeed, apart from the inner source identified in Sect. 3.1, we detected four additional sources. We extracted their astrometry by fitting a 2D Gaussian model directly to the sources in the derotated frames.

The astrometric measurements of HD 135344 Ab are listed in Table 2 and shown in Fig. 3 together with the suspected background sources. In this figure, the astrometry is displayed relative to the first epoch, showing that the planet moves mostly in eastward direction, whereas the background sources move in northeast direction. The direction of the background sources matches with the stationary track, but it shows that the proper motions of the background sources are not negligible. This is also seen in the sample of Gaia sources, from which we adopted

⁴ <https://www.eso.org/sci/facilities/paranal/instruments/gravity/tools.html>

⁵ <https://gitlab.obspm.fr/mnowak/exogravity.git>

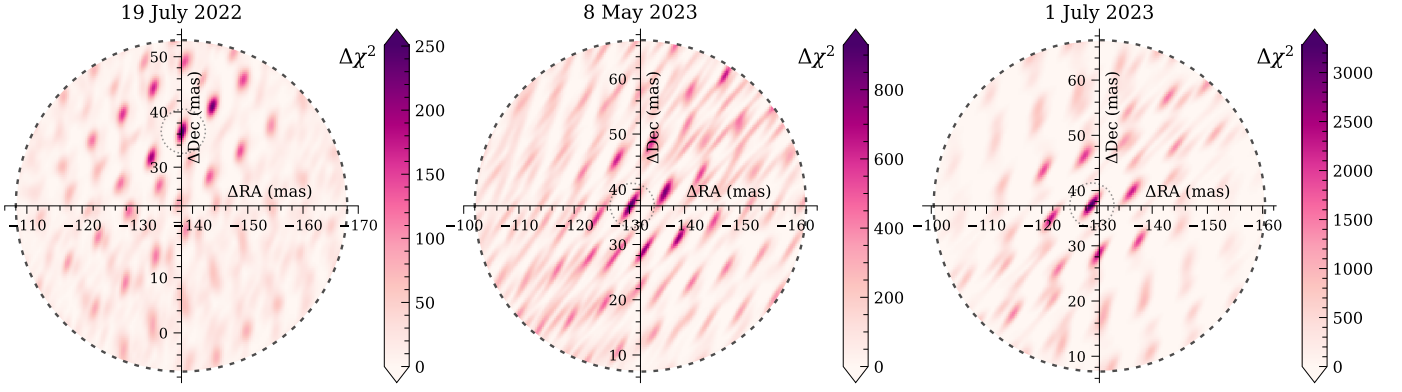


Fig. 2: Detections of HD 135344 AB with VLT/IRDIS. The color scale of the detection maps shows $\Delta\chi^2 = \chi_{\text{no planet}} - \chi_{\text{planet}}$. The intersection of the axes is at the center of the fiber, which has a field of view of ≈ 60 mas. For each observations the feature with the highest likelihood is encircled, which corresponds to the planet position. The planet position was 13 mas north from the fiber center during the first observation. The night of the observations are shown at the top of each panel.

Table 2: Astrometry of HD 135344 Ab.

| UT date ^a | MJD | Instrument | ΔRA^b (mas) | ΔDec^c (mas) | ρ^d |
|----------------------|----------|--------------|------------------------------|-------------------------------|----------|
| 2019 May 09 | 58612.2 | SPHERE/IRDIS | -161.6 ± 2.7 | 31.6 ± 1.3 | -0.33 |
| 2019 Jul 06 | 58670.0 | SPHERE/IRDIS | -162.0 ± 2.0 | 28.2 ± 1.3 | -0.17 |
| 2021 Jul 16 | 59412.0 | SPHERE/IRDIS | -144.8 ± 1.9 | 36.1 ± 1.2 | -0.22 |
| 2022 May 04 | 59703.2 | SPHERE/IRDIS | -142.3 ± 5.2 | 35.8 ± 2.0 | -0.58 |
| 2022 Jul 19 | 59779.06 | GRAVITY | -138.21 ± 0.15 | 36.34 ± 0.17 | -0.58 |
| 2023 May 08 | 60072.15 | GRAVITY | -130.41 ± 0.20 | 37.00 ± 0.28 | -0.95 |
| 2023 Jul 01 | 60126.98 | GRAVITY | -129.07 ± 0.13 | 37.36 ± 0.08 | -0.97 |

Notes. ^(a) UT date at the start of the observations. ^(b,c) Coordinates, RA and Dec, relative to the star HD 135344 A. ^(d) The Pearson correlation coefficient, ρ , quantifies the correlation between the uncertainties of ΔRA and ΔDec .

the proper motions to create a sample of non-stationary background stars.

From this comparison, we can conclude that the relative astrometry of the IRDIS background sources is approximately consistent with the population of Gaia sources. Here, we did not take into account differences in parallax, which we expect to be the reason that the IRDIS background sources do not match exactly with the bulk of the Gaia sources. There might also be systematics in the astrometry, such as the true north uncertainty, which has a larger impact on sources far from the on-axis science target.

The planet appears to move distinctly from the background sources, although somewhat in the same direction, which seemed initially suspicious. For the bulk of the Gaia sources, their simulated positions differ by more than 100 mas from the position of the planet with the last epoch. There are however a few outliers in the sample that have proper motions with a magnitude and direction similar to HD 135344 A, yielding a probability of $\sim 0.1\%$ that the putative planet is instead a background star with an unusually high proper motion. Considering and ruling out such a peculiar proper motion scenario is important, as shown by Nielsen et al. (2017) for the case of HD 131399 A.

3.3. Ruling out a non-stationary background star

The analysis in Sect. 3.2 shows that the astrometric measurements are difficult to explain with a background star. In this section, we will statistically explore the scenario of a background (or foreground) object, by fitting the relative astrometry of HD 135344 Ab with a non-stationary background model. We used *backtracks*⁶ (Balmer et al. 2025) to determine the coordinates, proper motion, and parallax, that best describe the astrometry as a background object. It uses dynamic nested sampling with the *dynesty* package for estimating the parameter posteriors (Speagle 2020). At the start, the Gaia catalog is queried for the parallaxes and proper motions of sources within a 0.2 deg window centered on HD 135344 A, which are used as normal distributed priors with the Bayesian inference: $\varpi_{\text{Gaia}} = 0.4 \pm 0.8$ mas, $\mu_{\text{RA,Gaia}} = -5.1 \pm 5.6$ mas yr⁻¹, $\mu_{\text{Dec,Gaia}} = -3.8 \pm 4.2$ mas yr⁻¹. We note that a similar sample was used for the proper motions applied in Fig. 3.

Figure 4 shows a random selection of posterior background tracks in comparison with the astrometry. The tracks are close to linear because the inferred parallax, $\varpi = 7.5 \pm 0.1$ mas, of the modeled background source is consistent with the parallax of HD 135344 Ab, $\varpi_* = 7.41 \pm 0.04$ mas. This result is in particular driven by the linear displacement of the GRAVITY astrometry that were obtained about two months apart. Specifically, the

⁶ <https://github.com/wbalmer/backtracks>

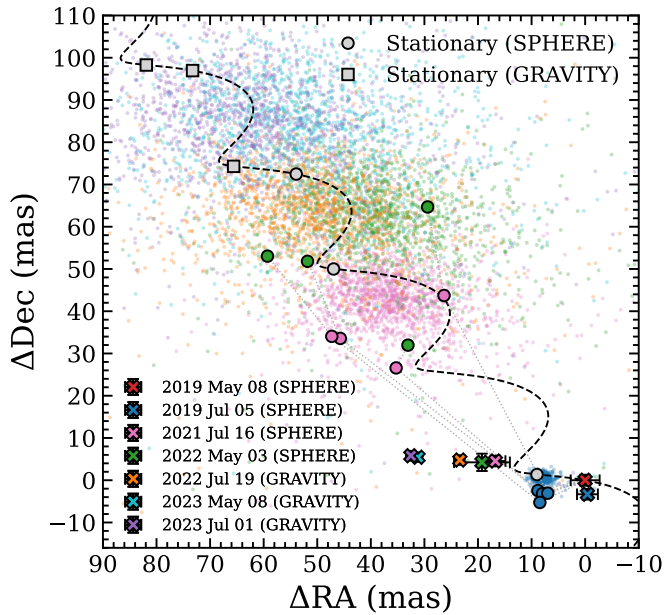


Fig. 3: Astrometric measurements relative to the first epoch (2019 May 08). The crosses are the positions of HD 135344 Ab, which is moving in eastward direction. The colored circles are the positions of the suspected background sources in the IRDIS field of view, which are connected with dotted lines between epochs. The dashed line is the track for a stationary background source, with the gray circles and squares indicating the three SPHERE and three GRAVITY epochs, respectively, after the initial detection. The small dots are a sample of Gaia sources within 0.1 deg from HD 135344 A (see main text for details). Colors indicate a specific epoch, for example, all markers with an orange color correspond to the 16th of July 2021.

high-precision measurements rule out a helix shape by a heliocentric parallax of a background star. As far as we know, this is the first confirmation of a directly imaged planet by a common parallax.

The retrieved proper motion, $\mu_{RA} = -9.0 \pm 0.1$ and $\mu_{Dec} = -22.9 \pm 0.1$ mas yr⁻¹, further confirms that the object is comoving with HD 135344 A. While μ_{RA} is consistent with the prior distribution from Gaia, which can also be noticed in Fig. 3, μ_{Dec} on the other hand is a 4.5σ outlier with respect to the Gaia sources. Therefore, the analysis shows that the object is most consistent with the proper motion of HD 135344 A. The difference is attributed to the orbital motion, which is approximately linear in eastward direction. The background fit utilized the proper motion parameter to mimic the orbital movement, hence the difference with in particular the RA component of the star's proper motion, $\mu_{RA,*} = -18.74 \pm 0.05$ mas yr⁻¹ and $\mu_{Dec,*} = -24.01 \pm 0.04$ mas yr⁻¹ (Gaia Collaboration et al. 2023).

To further quantify the significance, we list in Table 3 the Bayesian evidence (i.e., the marginalized likelihood), $\ln \mathcal{Z}$, for three cases of the background fit. For the stationary model, we fixed the parallax and proper motion to zero. The parameter estimation informed by the Gaia priors is the fit that we described earlier in this section. For comparison, loosening the priors to uniform distributions, increases $\ln \mathcal{Z}$ because the measurements did not match with the bulk of the Gaia sample. Instead, as a teaser for the next section, the Bayes factor of the model comparison between orbit and background fit is at least $\Delta \ln \mathcal{Z} = 30.0$,

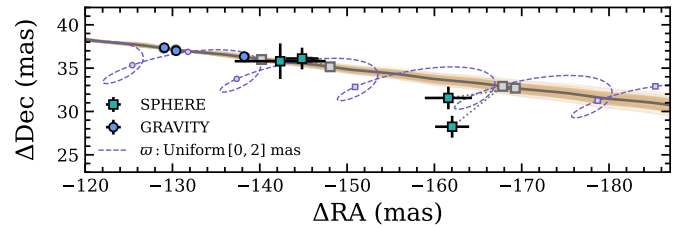


Fig. 4: Background fit of the relative astrometry. The important take-away is that the tracks are close to linear because the best-fit off-axis source has a common parallax with HD 135344 A, while the proper motion parameter mimics the approximate linear orbital movement. The figure shows 200 randomly drawn background tracks from the posterior. The track calculated from the median parameters is shown as gray solid line. The astrometric measurements are shown with colored markers and their respective epochs of the best-fit model are shown with gray markers. For comparison, the blue dashed line shows the best-fit model when using a parallax prior that forces the source to the background (≥ 500 pc).

Table 3: Bayesian evidence

| Model | $\ln \mathcal{Z}$ |
|----------------------------|---------------------|
| Keplerian orbit | -34.6 ± 0.1 |
| Background: uniform priors | -64.6 ± 0.2 |
| Background: Gaia priors | -81.9 ± 0.2 |
| Background: stationary | -272642.7 ± 0.1 |

so altogether we conclude that there is strong evidence that the source is co-moving with and orbiting around HD 135344 A.

3.4. Orbital analysis

The discovered planet shows clear orbital movement, possibly even with a slight curvature, so we carried out a fit with *orbitize*⁷ (Blunt et al. 2020) to infer its orbital elements. The posterior distributions were sampled with the nested sampling algorithm from MultiNest (Feroz & Hobson 2008; Buchner et al. 2014), while marginalizing over the parallax and system mass (see Table A.1). We used 2000 live points and restricted the priors on the argument of periastron, ω , and longitude of the ascending node, Ω , to one of the two solutions.

Figure 5 shows the posterior orbits and the credible regions are provide in Table 5. We retrieved a semi-major axis of $a \approx 17$ au, corresponding to a period of $P = 45_{-8}^{+11}$ yr. The eccentricity is hardly constrained and is negatively correlated with the inclination, which is a common outcome of fitting astrometry that covers a small fraction of the orbit (Ferrer-Chávez et al. 2021). This can also be seen in Fig. 5: circular orbits are symmetric with respect to the star whereas eccentric orbits have a smaller periastron. The orientation of the orbit on the sky is set by the inclination, $i \approx 74$ deg, and the longitude of the ascending node, $\Omega \approx 95$ deg. Since we only fit relative astrometry, there is a second solution for Ω and ω with a ≈ 180 deg difference. Finally, the disk of HD 135344 B is seen close to face-on ($i_{\text{disk}} \approx 20$ deg; e.g. Pérez et al. 2014), so the orbit of HD 135344 Ab is not coplanar with that the disk of the secondary star.

⁷ <https://github.com/sblunt/orbitize>

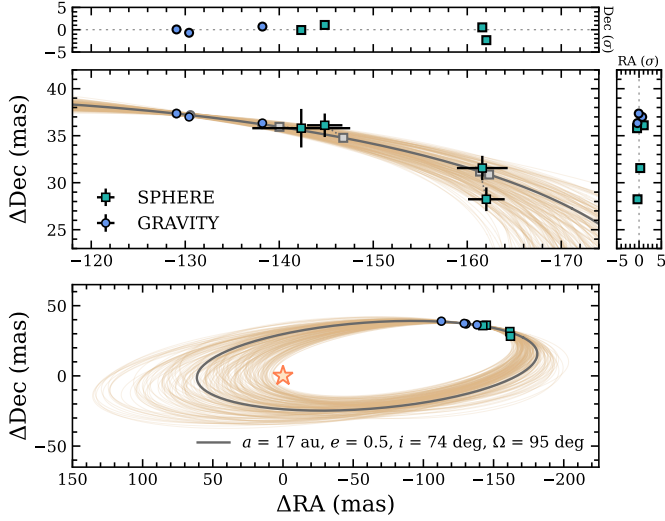


Fig. 5: Orbit fit of the relative astrometry. The bottom panel shows the full orbits and the top panel a zoom to the observation epochs. Both panels show the same 200 orbit samples that are randomly drawn from the posterior. The orbit with the highest likelihood is shown as gray solid line and the residuals of the best fit are normalized by the data uncertainties. The astrometric measurements are shown with colored markers, and their respective epochs of the best-fit model are shown with gray markers and connected with dotted lines. The planet is moving in counterclockwise direction.

3.5. Photometric analysis

The contrast measurements and calibrated photometry are listed in Table 4, both as magnitudes and fluxes. The dual-band imaging with SPHERE in the $H23$ and $K12$ bands enabled photometric characterization of the planet, for which we adopted the magnitudes from 2021 and 2022, because these data were obtained with a dedicated strategy for optimized accuracy of the flux calibration (see Sect. 2.1). Figure 6 shows a color-magnitude diagram that was created with the *species*⁸ toolkit (see Stolker et al. 2020 for details). In the figure, HD 135344 Ab is compared with late-type field objects, other directly imaged companions, and synthetic photometry from models. The isochrones, that were used for the calculation of the synthetic fluxes, were interpolated from the AMES-Cond and AMES-Dusty grids. These are evolutionary models with a cloudless and cloudy atmospheres, respectively, as boundary condition for the interior structure (Chabrier et al. 2000; Allard et al. 2001; Baraffe et al. 2003).

The absolute flux and color of HD 135344 Ab are consistent with the field objects that have a mid L spectral type. The photospheric temperature of L-type giant planets and brown dwarfs allows for the condensation of refractory species, hence their dusty atmospheres cause a red photometric appearance compared to cloudless atmospheres. The atmospheric reddening by clouds is typically stronger for young objects because their lower surface gravity (e.g., HIP 65426 b; Chauvin et al. 2017). The $H2-K1$ color of HD 135344 Ab is not unusually red and consistent with the field objects, although in particular similar with the reddest objects of that sample. At an age of 12 Myr (i.e., the pre-main-sequence age of HD 135344 B), the $H2$ luminosity of HD 135344 Ab is consistent with a planetary-mass object of

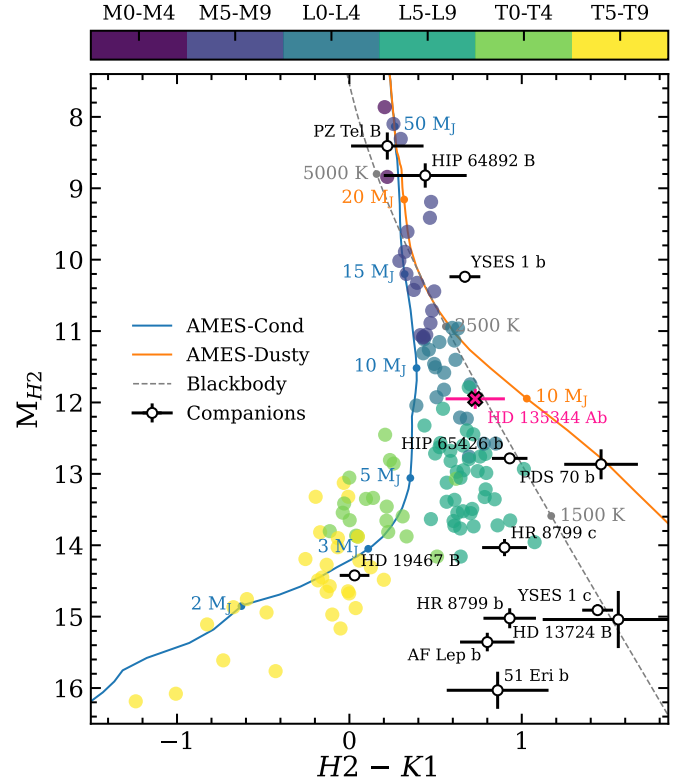


Fig. 6: Color-magnitude diagram of M_{H2} versus $H2 - K1$. The field objects are color-coded by M, L, and T spectral types (see discrete colorbar), and the directly imaged companions are labeled individually. HD 135344 Ab is highlighted with a pink cross. The blue and orange lines show the synthetic colors computed from the AMES-Cond and AMES-Dusty evolutionary tracks at an age of 12 Myr. Blackbody emission is shown for an object with a radius of $1 R_J$ (black dashed line).

$\approx 10 M_J$. We will provide a statistical inference of the planet's mass in Sect. 3.7.

3.6. Atmospheric modeling

The spectral appearance and inferred atmospheric parameters provide further insight into the nature of HD 135344 Ab. We compiled the near-infrared SED in Fig. 7 by combining the SPHERE and GRAVITY data. We used the Bayesian framework of the *species* toolkit (Stolker et al. 2020) to fit the data with an atmospheric model, specifically, by interpolating a grid of synthetic spectra from Sonora Diamondback (Morley et al. 2024). This is a radiative-convective equilibrium model that accounts for the condensation of refractory species into cloud particles. The vertical density profile of the cloud deck is parameterized by the sedimentation efficiency, f_{sed} . The model uses chemical equilibrium, which is a reasonable assumption in the temperature regime of HD 135344 Ab where CO will be the dominant carbon-bearing species. The parameter estimation was done with the nested sampling algorithm from MultiNest (Feroz & Hobson 2008; Buchner et al. 2014), using 2000 live point and accounting for the spectral covariances.

The photometry and spectra are compared with the best-fit model spectrum in Fig. 7, which has a goodness-of-fit statistic of $\chi^2_\nu = 1.3$. The IFS spectra are of low S/N (see Sect. 2.1) but the

⁸ <https://github.com/tomasstolker/species>

Table 4: Photometry of HD 135344 Ab.

| UT date | Filter | Contrast (mag) | App. magnitude (mag) | Flux (W m ⁻² μm ⁻¹) |
|-------------|-----------------|-------------------|-------------------------|---|
| 2019 May 09 | IRDIS <i>H2</i> | 10.17 ± 0.10 | 17.76 ± 0.11 | 1.02 ± 0.10 × 10 ⁻¹⁶ |
| | IRDIS <i>H3</i> | 10.05 ± 0.12 | 17.63 ± 0.12 | 9.66 ± 1.07 × 10 ⁻¹⁷ |
| 2019 Jul 06 | IRDIS <i>H2</i> | 9.95 ± 0.11 | 17.54 ± 0.11 | 1.24 ± 0.13 × 10 ⁻¹⁶ |
| | IRDIS <i>H3</i> | 9.83 ± 0.08 | 17.41 ± 0.08 | 1.18 ± 0.09 × 10 ⁻¹⁶ |
| 2021 Jul 16 | IRDIS <i>H2</i> | 10.01 ± 0.13 | 17.60 ± 0.14 | 1.17 ± 0.15 × 10 ⁻¹⁶ |
| | IRDIS <i>H3</i> | 9.79 ± 0.09 | 17.37 ± 0.09 | 1.23 ± 0.10 × 10 ⁻¹⁶ |
| 2022 May 04 | IRDIS <i>K1</i> | 9.30 ± 0.10 | 16.87 ± 0.10 | 8.49 ± 0.81 × 10 ⁻¹⁷ |
| | IRDIS <i>K2</i> | 8.89 ± 0.13 | 16.45 ± 0.13 | 9.65 ± 1.16 × 10 ⁻¹⁷ |

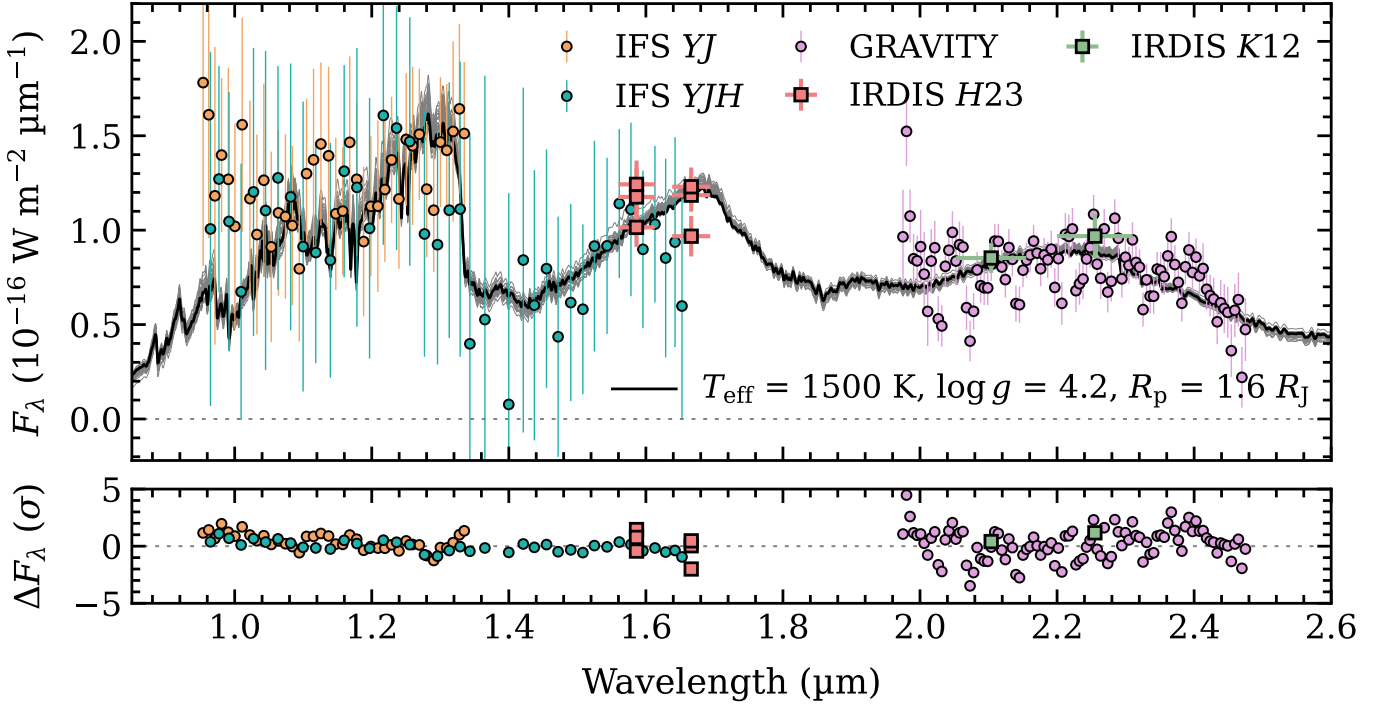


Fig. 7: Near-infrared spectral energy distribution of HD 135344 Ab. The black line is the best-fit model spectrum from Sonora Diamondback and the gray lines are 30 random samples from the posterior distribution, both shown at $R = 500$. The SPHERE/IFS and GRAVITY spectra are shown with circular markers, with the latter downsampled for clarity. The SPHERE/IRDIS photometry are shown with square markers. Their horizontal error bars indicate the FWHM of the filter profiles. The bottom panel shows the residuals of the best-fit model, calculated at the resolution and wavelength sampling of the data.

broad H₂O absorption feature between the *J* and *H* bands is visible in the *YJH* spectrum. Also the GRAVITY spectrum shows slopes in the pseudo-continuum that are expected to be caused by H₂O opacities. Tentatively, there could be a detection of the CO bandheads in the *K* band, but the GRAVITY spectrum also shows correlated noise appearing with a frequency and amplitude that could mimic the CO bands. Indeed, the initial residuals showed that the systematics were not fully accounted for by the covariances, so we fitted an uncertainty inflation for the GRAVITY spectrum, which yielded a $10 \pm 2\%$ increase relative to the model fluxes. From the photometry, the *H3* flux of the first epoch is in particular discrepant with the best-fit model, possibly due to the poorer observing conditions and not having the continuous satellite spots for the calibration (see Sect. 2.1).

The inferred parameters are listed in Table 5. The temperature, $T_{\text{eff}} \approx 1510$ K, is consistent with an mid L-type object, as empirically estimated from the *H2* brightness in Fig. 6. The surface gravity, $\log g$, and metallicity, $[M/H]$, are challenging to constrain from the low-resolution spectra since it requires a highly accurate calibration, while the parameters can be easily biased otherwise. We therefore adopted the constraint from the evolution fit, $\log g = 4.1 \pm 0.1$ (see Sect. 3.7), as normal prior for the atmospheric fit. The likelihood of the metallicity peaked at the super-solar edge of the model grid, but the data are also consistent with solar abundances. The low sedimentation parameter clearly favors a dusty atmosphere while we can rule out an atmosphere with strongly settled clouds. Rerunning the fit with a fixed sedimentation parameter of $f_{\text{sed}} = 8$ yielded a Bayes factor

Table 5: Planet parameters of HD 135344 Ab.

| Parameter | Value | Units |
|----------------------------------|-------------------------|-------|
| <i>Orbit fit</i> | | |
| a | $16.5^{+2.8}_{-2.0}$ | au |
| e | $0.5^{+0.2}_{-0.2}$ | |
| i | $73.6^{+2.8}_{-4.7}$ | deg |
| Ω^a | $94.9^{+1.8}_{-3.1}$ | deg |
| ω^b | $8.2^{+8.7}_{-10.8}$ | deg |
| t_p | 65405^{+2026}_{-1378} | MJD |
| <i>Atmosphere fit</i> | | |
| T_{eff} | 1510^{+35}_{-35} | K |
| $\log g$ | $4.14^{+0.06}_{-0.07}$ | dex |
| [M/H] | $\gtrsim 0.0$ | dex |
| f_{sed} | $\lesssim 1.5$ | |
| R_p | $1.60^{+0.07}_{-0.06}$ | R_J |
| A_V | $\lesssim 0.5$ | mag |
| <i>Evolution fit^c</i> | | |
| Age | 12^{+3}_{-4} | Myr |
| M_p | $10.0^{+1.4}_{-1.9}$ | M_J |
| T_{eff} | 1585^{+82}_{-73} | K |
| $\log g$ | $4.1^{+0.1}_{-0.1}$ | dex |
| R_p | $1.45^{+0.06}_{-0.03}$ | R_J |

Notes. The listed values are the median, and the 16th and 84th percentiles from the posterior distributions, only accounting for statistical uncertainties. Lower and upper limits are provided as the 16th and 84th percentile, respectively. ^(a,b) The table includes one solution for ω and Ω , but there is a second solution with an offset of 180 deg. ^(c) The age and planet mass were free parameters, whereas T_{eff} , R , and $\log g$ have been interpolated from the evolutionary grid based on the posterior samples.

of $\Delta \ln \mathcal{Z} = 43$ relative to the model in which f_{sed} was a free parameter.

From the T_{eff} and R posterior, we computed the bolometric luminosity, $\log L/L_{\odot} = -3.9 \pm 0.1$. We note that the statistical uncertainty on the luminosity was only ≈ 0.01 dex, so we reran the spectral fit using four other cloudy models: ExoREM (Charnay et al. 2018), petitCODE (Mollière et al. 2015), DRIFT-PHOENIX (Helling et al. 2008), BT-Settl (Allard et al. 2012), AMES-Dusty (Allard et al. 2001). The deviation on the retrieved luminosity, $\Delta \log L/L_{\odot} \approx 0.1$ dex, was adopted as approximate systematic uncertainty. In the next section, we will use the luminosity to quantify the mass of the planet.

3.7. Bulk parameters and evolutionary constraints

In Sect. 3.5, we showed that the H -band luminosity of HD 135344 Ab is consistent with a dusty, mid L-type object with an approximate mass of $10 M_J$. We will now quantify the mass and other bulk parameters using an evolutionary model. To do so, we use again the species toolkit (Stolker et al. 2020), this time fitting the bolometric luminosity, $\log L/L_{\odot} = -3.9 \pm 0.1$, that we inferred from the atmospheric modeling (see Sect. 3.6), with a grid of evolutionary tracks which is interpolated as function of mass and age. The age of the system is applied as asymmetric normal prior by adopting the pre-main sequence age of HD 135344 B, $11.9^{+3.7}_{-5.8}$ Myr (Garufi et al. 2018). Similar to the

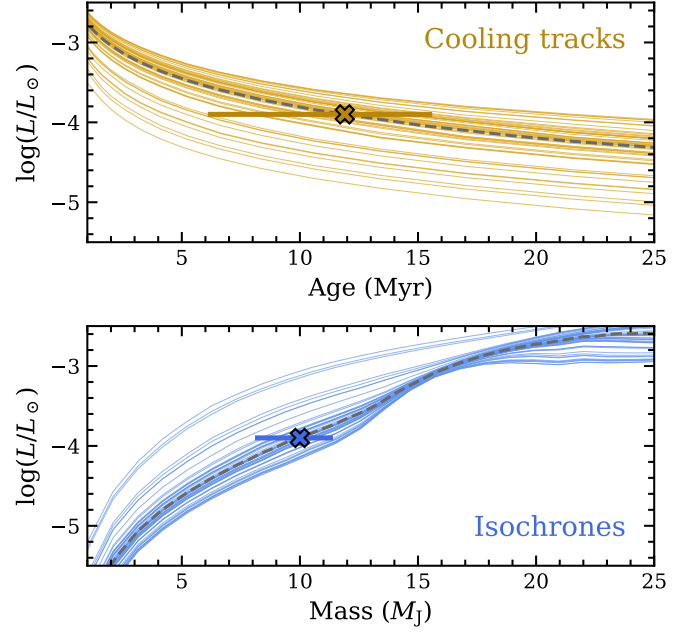


Fig. 8: Cooling tracks and isochrones inferred from the planet’s luminosity. The colored lines are 50 random samples from the posterior distribution, showing the cooling tracks and isochrones in the top and bottom panel, respectively, and the best-fit model as dashed line in each panel. The crosses are the luminosity of HD 135344 Ab, $\log L/L_{\odot} = -3.9 \pm 0.1$, and the horizontal error bars indicate the prior age and posterior mass in the top and bottom panel, respectively.

spectral fit, a main limitation here are non-linear variations in the model grid, which could lead to inaccuracies and underestimated uncertainties. For the fit, we used the ATMO model (Phillips et al. 2020) because the cooling tracks seemed reasonably spaced to be interpolated. The parameter estimation was done with MultiNest (Feroz & Hobson 2008; Buchner et al. 2014) and using 1000 live points.

The mass and evolutionary constraints are presented in Fig. 8, showing both the isochrones and cooling tracks that best describe the luminosity and age of HD 135344 Ab. We inferred a mass of $M \approx 10 M_J$ and the age is consistent with the prior but slightly more constrained (see Table 5). After the fit, we interpolated the evolutionary grid once more for each mass-age sample, in order to extract the related temperature, $T_{\text{eff}} \approx 1585$, surface gravity, $\log g \approx 4.1$, and radius, $R \approx 1.5$. Table 5 shows that the inferred bulk parameters are, within the considered credible regions, consistent with the parameter values estimated with the spectral modeling in Sect. 3.6, suggesting that the results are robust given that there were two different, although correlated, approaches used. The exception is the radius which differs by 2σ between the atmospheric and evolution fit.

4. Discussion and conclusions

We have reported on the direct discovery of a young giant planet at the A0V type star HD 135344 A. The planet was detected through high-contrast imaging and interferometric observations. Careful astrometric analysis of seven datasets, with a total baseline of four years, shows that the object is co-moving with the central star, confirmed both by a common parallax and common proper motion. The inferred atmospheric and bulk param-

ters point to a planetary nature, with a model-dependent mass of $M \approx 10 M_J$. The planet position changed by ≈ 30 mas and shows a slight curvature, yielding a constraint on the orbit's semi-major axis of approximately 15–20 au.

Adopting the pre-main-sequence age of ≈ 12 Myr from the secondary star, HD 135344 Ab might be the youngest directly imaged planet that has fully formed and orbits on solar system scales. Figure 9 shows a comparison with the ages and semi-major axes of other close-in directly imaged planets. Young directly imaged planets at small separations (≤ 100 au) have only been detected orbiting at intermediate mass stars. The planets in Fig. 9 are all orbiting A- and F-type stars, so the discovery of HD 135344 Ab at an A0 type star follows that trend. This contrasts young planetary-mass objects on wide orbits (≥ 100 au), which are typically found at late type stars (e.g., Bowler et al. 2014). Given the relatively small orbit of HD 135344 Ab, this planetary-mass companion is expected to have formed in a protoplanetary disk, instead of being the low-mass tail of binary star formation. In fact, the current planet location might be in the vicinity of the approximate snowline location for the spectral type of the host star (see Fig. 9), although the planet may have migrated during its formation phase.

Apart from the age constraint from HD 135344 B, there is a recent work by Ratzenböck et al. (2023), who used a clustering algorithm to map the star formation history of Sco-Cen. HD 135344 AB was associated with the ϕ Lup group in UCL, for which an isochrone age of ≈ 10 and ≈ 17 Myr was determined with two evolutionary models. An age of 10 Myr would match best with the pre-main-sequence age of HD 135344 B. Arguably, it would also be more consistent with the high IR excess of the secondary star. Maintaining a dust-rich disk up to 17 Myr would be (even more) puzzling. If the system were to be ≈ 17 Myr then the planet mass would still be in the planetary regime, $M_p \approx 12 M_J$, but close to the deuterium-burning limit.

In contrast to the secondary star, the circumstellar environment of HD 135344 A is already depleted, given the minor IR excess (see Appendix A). This is also consistent with a non-detection of a disk in scattered light in the SPHERE imagery. The origin of the different disk evolution timescales of the primary and secondary star is not known, but could be related to a more efficient photoevaporation by the stronger radiation field of HD 135344 A. Indeed, disk lifetimes are known to increase towards later spectral types (e.g., Luhman 2022). During the early evolution of the system, the primary star was likely a Herbig Ae star with a protoplanetary disk in which HD 135344 Ab would have carved a wide gap during its formation. Dust- and gas-depleted cavities and gaps are quite common at Herbig Ae stars (e.g., van der Marel & Mulders 2021). Such resolved substructures are signposts for forming planets, but only a few gap-carving planets have been detected (e.g., PDS 70 b/c; Keppler et al. 2018; Haffert et al. 2019). The discovery of close-in, directly imaged planets such as HD 135344 Ab shows that Jovian planets might indeed be responsible for some of the large cavities. Possibly they are more difficult to detect during formation as the dust has not yet been dispersed, since even cavities are not fully cleared from small dust.

HD 135344 Ab will be an appealing target for spectral characterization with the next generation of large ground-based telescope facilities (e.g., Brandl et al. 2010), given its small angular and physical separation with the star. The quality of the current measurements was sufficient to identify H₂O absorption in the low-resolution spectra and to infer the bulk parameters. Spectral inference of molecular abundances will be more challenging given the planet's brightness, but might be feasible

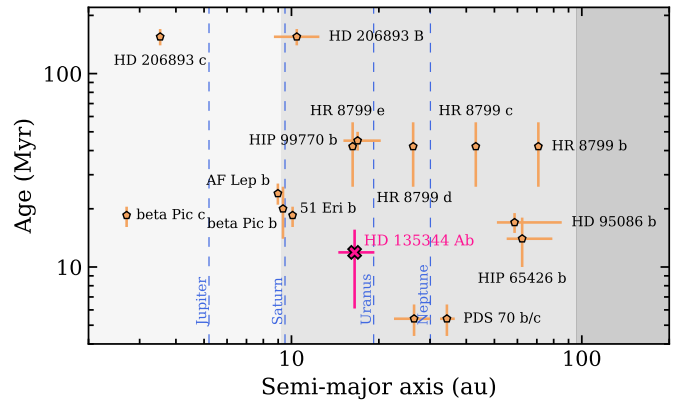


Fig. 9: Age versus semi-major axis of directly imaged planets. We selected young companions with planetary masses (except HD 206893 B), $M \leq 13 M_J$, planet-to-star mass ratios of $q \leq \frac{1}{25}$, and orbits smaller than ≈ 100 au. The locations of the giant planets in the solar system are indicated with vertically dashed lines and the gray areas are, from left to right, separated by the approximate locations of the H₂O and CO₂ icelines of an A0 type star (Öberg et al. 2011). Semi-major axes have been retrieved from whereistheplanet when available (Wang et al. 2021a), and from Wang et al. (2021b), Hinkley et al. (2023), Currie et al. (2023), and De Rosa et al. (2023) otherwise. The ages have been adopted from Pecaut et al. (2012), Bell et al. (2015), Macintosh et al. (2015), Chauvin et al. (2017), Müller et al. (2018), Garufi et al. (2018), Zuckerman (2019), Miret-Roig et al. (2020), Brandt et al. (2021), and Hinkley et al. (2023). Systematic uncertainties on the ages (e.g. due to uncertain cluster membership) are not reflected by the error bars.

with KPIC, the fiber-fed high-resolution infrared spectrograph at Keck (Wang et al. 2024), or with the enhanced sensitivity of the recent upgrade to GRAVITY+ (Gravity+ Collaboration et al. 2022). Extending the SED from NIR to MIR wavelengths will increase the accuracy on the bolometric luminosity and other bulk parameters, and so will the extraction and calibration at short NIR wavelengths. Specifically, the fluxes at the blue end ($\lambda \leq 1.1 \mu\text{m}$) of the IFS spectrum are systematically higher than the model spectra in Fig. 7. We suspect that this is a bias in the spectral extraction, possibly due to the lower planet contrast, enhanced speckle noise, and/or reduced instrument transmission at the shortest wavelengths. Similar contaminating systematics are also seen at the short wavelengths in the IFS spectra of other faint planets (e.g. Samland et al. 2017). The effect did however not impact the parameter estimation given the S/N of the spectra. Since the inferred luminosity is consistent with a planet mass of $M \approx 10 M_J$, but the R_p from the spectral fit is a bit too large given the mass and age constraint, this could imply that the T_{eff} and R_p inferred from the SED are somewhat under- and over-estimated, respectively.

The orbital analysis yielded first constraints on the elements, given that the astrometry covers about 9% of the orbital period, $P \approx 45$ yr. The semi-major axis has a precision of ≈ 2 –3 au, but is correlated with the poorly constrained eccentricity, and therefore also with the inclination. The posterior favors low to intermediate eccentricities, while face-on orbits with high eccentricities are ruled out, but this is to be confirmed with astrometric monitoring. The projected motion will be somewhat linear during the coming years, while the curvature will increase again towards

periastron, which is in the year 2038.5 ± 4.4 . Since the planet orbit has an high inclination, we can conclude that the orbit is misaligned with the protoplanetary disk of the secondary star in the HD 135344 AB binary system, as it is seen close to face-on ($i_{\text{disk}} \approx 20$ deg; e.g. Pérez et al. 2014). This is also not surprising given the large projected separation between the two stars (≈ 2800 au), so their circumstellar environments are expected to have evolved independently.

The star was not observed by Hipparcos so a proper motion anomaly cannot be determined. It will be interesting to analyze the astrometric measurements from Gaia DR4. Although the orbital period of HD 135344 Ab is ~ 45 years, whereas the baseline of DR4 is 5.5 years, an acceleration of the star's proper motion might be detectable. Including the absolute astrometry in the orbit fit will place a first constraint on the dynamical mass, which will be valuable given the early evolutionary stage of the planet and its possible formation in a protoplanetary disk. Furthermore, combined analysis of the absolute and relative astrometry could place constraints on the multiplicity of the planetary system, since close-in directly imaged planets are often found in pairs or more (e.g. at β Pic, HR 8799, HD 206893, PDS 70).

The detection of HD 135344 Ab at only $3-4\lambda/D$ demonstrates the powerful high-contrast and high-resolution capabilities of the SPHERE and GRAVITY instrument. This study also highlights the importance of high-precision astrometric measurements to fully disentangle orbital from background motion in a region of non-stationary background stars. However, there was a good portion of luck involved with the discovery of HD 135344 Ab, since we caught the planet at a favorable separation along its inclined orbit. The coming 10 to 20 years, the angular separation with its star is decreasing down to $\approx 10-35$ mas, so the planet would not have been discovered with SPHERE for a large fraction of its orbit.

Finally, direct imaging surveys have established that giant planets are rare at separations ≥ 20 au (Nielsen et al. 2019; Vigan et al. 2021). The detection rate is however expected to increase towards shorter separations, where radial velocity surveys have revealed a turnover point in the occurrence rates (Fernandes et al. 2019; Fulton et al. 2021). Gaia DR4 may reveal hints of similar close-in giant planets in star forming regions, guiding direct imaging searches and post-processing algorithms (e.g., Currie et al. 2023; Winterhalder et al. 2024). HD 135344 Ab might be part of a population of giant planets that could have formed in the vicinity of the snowline, which have remained challenging to detect since most surveys and observing strategies have not been optimized for such small separations.

Acknowledgements. Based on observations collected at the European Southern Observatory under ESO programmes 0103.C-0189(A), 105.20A8.001, 109.22ZA.004, 1104.C-0651(G), and 111.24FS.001. T.S. acknowledges the support from the Netherlands Organisation for Scientific Research (NWO) through grant VI.Veni.202.230. J.J.W. is supported by NASA XRP Grant 80NSSC23K0280. S.L. acknowledges the support of the French Agence Nationale de la Recherche (ANR), under grant ANR-21-CE31-0017 (project ExoVLT). Part of this work was performed using the ALICE compute resources provided by Leiden University. This work used the Dutch national e-infrastructure with the support of the SURF Cooperative using grant no. EINF-1620. This research has made use of the Jean-Marie Mariotti Center Aspro service.

References

Allard, F., Hauschildt, P. H., Alexander, D. R., Tamanai, A., & Schweitzer, A. 2001, *ApJ*, 556, 357
 Allard, F., Homeier, D., & Freytag, B. 2012, *Philosophical Transactions of the Royal Society of London Series A*, 370, 2765
 Amara, A. & Quanz, S. P. 2012, *MNRAS*, 427, 948

Balmer, W. O., Otten, G. P. P. L., & Stolker, T. 2025, *backtracks: a python package to compare relative astrometry with background helical motion*
 Baraffe, I., Chabrier, G., Barman, T. S., Allard, F., & Hauschildt, P. H. 2003, *A&A*, 402, 701
 Bell, C. P. M., Mamajek, E. E., & Naylor, T. 2015, *MNRAS*, 454, 593
 Beuzit, J. L., Vigan, A., Mouillet, D., et al. 2019, *A&A*, 631, A155
 Blunt, S., Wang, J. J., Angelo, I., et al. 2020, *AJ*, 159, 89
 Bohlin, R. C., Gordon, K. D., & Tremblay, P. E. 2014, *PASP*, 126, 711
 Bowler, B. P., Liu, M. C., Kraus, A. L., & Mann, A. W. 2014, *ApJ*, 784, 65
 Brandl, B. R., Lenzen, R., Pantin, E., et al. 2010, in *Society of Photo-Optical Instrumentation Engineers (SPIE) Conference Series*, Vol. 7735, Ground-based and Airborne Instrumentation for Astronomy III, ed. I. S. McLean, S. K. Ramsay, & H. Takami, 77352G
 Brandt, G. M., Brandt, T. D., Dupuy, T. J., Michalik, D., & Marleau, G.-D. 2021, *ApJ*, 915, L16
 Brown, J. M., Blake, G. A., Qi, C., et al. 2009, *ApJ*, 704, 496
 Buchner, J., Georgakakis, A., Nandra, K., et al. 2014, *A&A*, 564, A125
 Chabrier, G., Baraffe, I., Allard, F., & Hauschildt, P. 2000, *ApJ*, 542, 464
 Charnay, B., Bézard, B., Baudino, J. L., et al. 2018, *ApJ*, 854, 172
 Chauvin, G., Desidera, S., Lagrange, A. M., et al. 2017, *A&A*, 605, L9
 Claudi, R. U., Turatto, M., Gratton, R. G., et al. 2008, in *Society of Photo-Optical Instrumentation Engineers (SPIE) Conference Series*, Vol. 7014, Ground-based and Airborne Instrumentation for Astronomy II, ed. I. S. McLean & M. M. Casali, 70143E
 Coulson, I. M. & Walthers, D. M. 1995, *MNRAS*, 274, 977
 Cugno, G., Leisenring, J., Wagner, K. R., et al. 2024, *AJ*, 167, 182
 Currie, T., Brandt, G. M., Brandt, T. D., et al. 2023, *Science*, 380, 198
 Cutri, R. M., Skrutskie, M. F., van Dyk, S., et al. 2003, *2MASS All Sky Catalog of point sources*
 De Rosa, R. J., Nielsen, E. L., Wahhaj, Z., et al. 2023, *A&A*, 672, A94
 Dohlen, K., Langlois, M., Saisse, M., et al. 2008, in *Society of Photo-Optical Instrumentation Engineers (SPIE) Conference Series*, Vol. 7014, Ground-based and Airborne Instrumentation for Astronomy II, ed. I. S. McLean & M. M. Casali, 70143L
 Fairlamb, J. R., Oudmaijer, R. D., Mendigutía, I., Ilee, J. D., & van den Ancker, M. E. 2015, *MNRAS*, 453, 976
 Fernandes, R. B., Mulders, G. D., Pascucci, I., Mordasini, C., & Emsenhuber, A. 2019, *ApJ*, 874, 81
 Feroz, F. & Hobson, M. P. 2008, *MNRAS*, 384, 449
 Ferrer-Chávez, R., Wang, J. J., & Blunt, S. 2021, *AJ*, 161, 241
 Fulton, B. J., Rosenthal, L. J., Hirsch, L. A., et al. 2021, *ApJS*, 255, 14
 Gaia Collaboration, Vallenari, A., Brown, A. G. A., et al. 2023, *A&A*, 674, A1
 Garufi, A., Benisty, M., Pinilla, P., et al. 2018, *A&A*, 620, A94
 Garufi, A., Quanz, S. P., Avenhaus, H., et al. 2013, *A&A*, 560, A105
 GRAVITY Collaboration, Abuter, R., Accardo, M., et al. 2017, *A&A*, 602, A94
 Gravity+ Collaboration, Abuter, R., Alarcon, P., et al. 2022, *The Messenger*, 189, 17
 GRAVITY Collaboration, Lacour, S., Nowak, M., et al. 2019, *A&A*, 623, L11
 GRAVITY Collaboration, Nowak, M., Lacour, S., et al. 2020, *A&A*, 633, A110
 Haffert, S. Y., Bohn, A. J., de Boer, J., et al. 2019, *Nature Astronomy*, 3, 749
 Helling, C., Dehn, M., Woitke, P., & Hauschildt, P. H. 2008, *ApJ*, 675, L105
 Hinkley, S., Lacour, S., Marleau, G. D., et al. 2023, *A&A*, 671, L5
 Hög, E., Fabricius, C., Makarov, V. V., et al. 2000, *A&A*, 355, L27
 Houk, N. 1982, *Michigan Catalogue of Two-dimensional Spectral Types for the HD stars. Volume 3. Declinations -40° to -26°*
 Keppler, M., Benisty, M., Müller, A., et al. 2018, *A&A*, 617, A44
 Lacour, S., Wang, J. J., Nowak, M., et al. 2020, in *Society of Photo-Optical Instrumentation Engineers (SPIE) Conference Series*, Vol. 11446, Optical and Infrared Interferometry and Imaging VII, ed. P. G. Tuthill, A. Mérand, & S. Sallum, 114460O
 Luhman, K. L. 2022, *AJ*, 163, 25
 Macintosh, B., Graham, J. R., Barman, T., et al. 2015, *Science*, 350, 64
 Maire, A. L., Stolker, T., Messina, S., et al. 2017, *A&A*, 601, A134
 Mason, B. D., Wycoff, G. L., Hartkopf, W. I., Douglass, G. G., & Worley, C. E. 2001, *AJ*, 122, 3466
 Miret-Roig, N., Galli, P. A. B., Brandner, W., et al. 2020, *A&A*, 642, A179
 Mollière, P., van Boekel, R., Dullemond, C., Henning, T., & Mordasini, C. 2015, *ApJ*, 813, 47
 Morley, C. V., Mukherjee, S., Marley, M. S., et al. 2024, *ApJ*, 975, 59
 Müller, A., Keppler, M., Henning, T., et al. 2018, *A&A*, 617, L2
 Muto, T., Grady, C. A., Hashimoto, J., et al. 2012, *ApJ*, 748, L22
 Nielsen, E. L., De Rosa, R. J., Macintosh, B., et al. 2019, *AJ*, 158, 13
 Nielsen, E. L., Rosa, R. J. D., Rameau, J., et al. 2017, *AJ*, 154, 218
 Nowak, M., Lacour, S., Lagrange, A. M., et al. 2020, *A&A*, 642, L2
 Öberg, K. I., Murray-Clay, R., & Bergin, E. A. 2011, *ApJ*, 743, L16
 Pécaut, M. J., Mamajek, E. E., & Bubar, E. J. 2012, *ApJ*, 746, 154
 Pérez, L. M., Isella, A., Carpenter, J. M., & Chandler, C. J. 2014, *ApJ*, 783, L13
 Phillips, M. W., Tremblin, P., Baraffe, I., et al. 2020, *A&A*, 637, A38
 Ratzenböck, S., Großschedl, J. E., Alves, J., et al. 2023, *A&A*, 678, A71
 Samland, M., Bouwman, J., Hogg, D. W., et al. 2021, *A&A*, 646, A24

- 660 Samland, M., Mollière, P., Bonnefoy, M., et al. 2017, *A&A*, 603, A57
 Siess, L., Dufour, E., & Forestini, M. 2000, *A&A*, 358, 593
 Speagle, J. S. 2020, *MNRAS*, 493, 3132
 Stolker, T., Bonse, M. J., Quanz, S. P., et al. 2019, *A&A*, 621, A59
 Stolker, T., Quanz, S. P., Todorov, K. O., et al. 2020, *A&A*, 635, A182
 Stolker, T., Sitko, M., Lazareff, B., et al. 2017, *ApJ*, 849, 143
 van der Marel, N. & Mulders, G. D. 2021, *AJ*, 162, 28
 Vigan, A. 2020, vlt-sphere: Automatic VLT/SPHERE data reduction and analysis, Astrophysics Source Code Library, record ascl:2009.002
 Vigan, A., Fontanive, C., Meyer, M., et al. 2021, *A&A*, 651, A72
 670 Vigan, A., Moutou, C., Langlois, M., et al. 2010, *MNRAS*, 407, 71
 Wang, J. J., Kulikaukas, M., & Blunt, S. 2021a, whereistheplanet: Predicting positions of directly imaged companions, Astrophysics Source Code Library, record ascl:2101.003
 Wang, J. J., Mawet, D., Xuan, J. W., et al. 2024, in Society of Photo-Optical Instrumentation Engineers (SPIE) Conference Series, Vol. 13096, Ground-based and Airborne Instrumentation for Astronomy X, ed. J. J. Bryant, K. Motohara, & J. R. D. Vernet, 130961X
 Wang, J. J., Vigan, A., Lacour, S., et al. 2021b, *AJ*, 161, 148
 Widmann, F., Gillessen, S., Ott, T., et al. 2022, in Society of Photo-Optical Instrumentation Engineers (SPIE) Conference Series, Vol. 12183, Optical and Infrared Interferometry and Imaging VIII, ed. A. Mérand, S. Sallum, & J. Sanchez-Bermudez, 121830U
 680 Winterhalder, T. O., Lacour, S., Mérand, A., et al. 2024, *A&A*, 688, A44
 Wright, E. L., Eisenhardt, P. R. M., Mainzer, A. K., et al. 2010, *AJ*, 140, 1868
 Zuckerman, B. 2019, *ApJ*, 870, 27
- 1 Leiden Observatory, Leiden University, Einsteinweg 55, 2333 CC Leiden, The Netherlands
 2 Max Planck Institute for Astronomy, Königstuhl 17, 69117 Heidelberg, Germany
 3 Department of Physics & Astronomy, Johns Hopkins University, 3400 N. Charles Street, Baltimore, MD 21218, USA
 4 Space Telescope Science Institute, 3700 San Martin Drive, Baltimore, MD 21218, USA
 5 Department of Astrophysics/IMAPP, Radboud University, Heyendaalseweg 135, 6525 AJ Nijmegen, The Netherlands
 6 European Southern Observatory, Karl-Schwarzschild-Straße 2, 85748 Garching, Germany
 7 LESIA, Observatoire de Paris, PSL, CNRS, Sorbonne Université, Université de Paris, 5 place Janssen, 92195 Meudon, France
 8 Center for Interdisciplinary Exploration and Research in Astrophysics (CIERA) and Department of Physics and Astronomy, Northwestern University, Evanston, IL 60208, USA
 9 Institute of Astronomy, University of Cambridge, Madingley Road, Cambridge CB3 0HA, United Kingdom
 10 Univ. Grenoble Alpes, CNRS, IPAG, 38000 Grenoble, France
 11 Department of Astrophysical & Planetary Sciences, JILA, Duane Physics Bldg., 2000 Colorado Ave, University of Colorado, Boulder, CO 80309, USA
 12 Anton Pannekoek Institute for Astronomy, University of Amsterdam, Science Park 904, 1098 XH Amsterdam, The Netherlands
 13 SRON Netherlands Institute for Space Research, Sorbonnelaan 2, 3584 CA Utrecht, The Netherlands
 14 Institute for Particle Physics and Astrophysics, ETH Zurich, Wolfgang-Pauli-Strasse 27, 8093 Zurich, Switzerland
 15 Universidade de Lisboa - Faculdade de Ciências, Campo Grande, 1749-016 Lisboa, Portugal
 16 CENTRA - Centro de Astrofísica e Gravitação, IST, Universidade de Lisboa, 1049-001 Lisboa, Portugal
 17 Max Planck Institute for extraterrestrial Physics, Giessenbachstraße 1, 85748 Garching, Germany
 18 Université Côte d’Azur, Observatoire de la Côte d’Azur, CNRS, Laboratoire Lagrange, Bd de l’Observatoire, CS 34229, 06304 Nice cedex 4, France
 19 Aix Marseille Univ, CNRS, CNES, LAM, Marseille, France
 20 STAR Institute, Université de Liège, Allée du Six Août 19c, 4000 Liège, Belgium
 21 1. Institute of Physics, University of Cologne, Zùlpicher Straße 77, 50937 Cologne, Germany
 22 Max Planck Institute for Radio Astronomy, Auf dem Hùgel 69, 53121 Bonn, Germany
 23 Universidade do Porto, Faculdade de Engenharia, Rua Dr. Roberto Frias, 4200-465 Porto, Portugal
 24 School of Physics, University College Dublin, Belfield, Dublin 4, Ireland
 25 Astrophysics Group, Department of Physics & Astronomy, University of Exeter, Stocker Road, Exeter, EX4 4QL, United Kingdom
 26 Departments of Physics and Astronomy, Le Conte Hall, University of California, Berkeley, CA 94720, USA
 27 European Southern Observatory, Casilla 19001, Santiago 19, Chile
 28 Advanced Concepts Team, European Space Agency, TEC-SF, ESTEC, Keplerlaan 1, NL-2201, AZ Noordwijk, The Netherlands
 29 University of Exeter, Physics Building, Stocker Road, Exeter EX4 4QL, United Kingdom
 30 Fakultät für Physik, Universität Duisburg-Essen, Lotharstraße 1, 47057 Duisburg, Germany
 31 Institut für Astronomie und Astrophysik, Universität Tùbingen, Auf der Morgenstelle 10, 72076 Tùbingen, Germany
 32 Astronomy Department, University of Michigan, Ann Arbor, MI 48109 USA
 33 Academia Sinica, Institute of Astronomy and Astrophysics, 11F Astronomy-Mathematics Building, NTU/AS campus, No. 1, Section 4, Roosevelt Rd., Taipei 10617, Taiwan
 34 European Space Agency (ESA), ESA Office, Space Telescope Science Institute, 3700 San Martin Drive, Baltimore, MD 21218, USA
 35 Department of Earth & Planetary Sciences, Johns Hopkins University, Baltimore, MD, USA
 36 Max Planck Institute for Astrophysics, Karl-Schwarzschild-Str. 1, 85741 Garching, Germany
 37 Excellence Cluster ORIGINS, Boltzmannstraße 2, D-85748 Garching bei Mùnchen, Germany
 38 The Kavli Institute for Astronomy and Astrophysics, Peking University, Beijing 100871, China

Appendix A: Stellar parameters

In this appendix, we analyze the spectral energy distribution (SED) of HD 135344 A. This is important for the calibration of the contrast measurements and, given the age of the system, to identify potential IR excess by circumstellar dust. Similar to fit of the near-infrared planet SED in Sect. 3.6, we used *species* (Stolker et al. 2020) to model the stellar SED and retrieve the atmospheric parameters, in this case using the BT-NextGen model spectra (Allard et al. 2012). The parameter posteriors were then used for computing synthetic photometry and spectra of the star, in order to convert the contrast to flux. The main stellar parameters are listed in Table A.

The parameter estimation is based on the low-resolution Gaia XP spectrum, and Gaia *G* and *G_{RVS}*, TYCHO *BV*, and 2MASS *JHK_s* photometry. We fitted an error bar inflation for the XP spectrum to account for the systematics that were seen as low-frequency oscillations in the spectrum. Similarly, we inflated the uncertainty of *G_{RVS}* flux. The best-fit model spectrum has a goodness-of-fit of $\chi^2_\nu = 0.94$ and is compared with the data in Fig. A.1. The WISE fluxes were not included in the fit since the residuals revealed excess emission starting at WISE *W3* ($\lambda_0 \approx 12 \mu\text{m}$) or perhaps already at *W2* ($\lambda_0 \approx 4.6 \mu\text{m}$). The WISE photometry is however flagged as possibly contaminated by a diffraction spike of the secondary star, which has a high IR excess. Also, the initial WISE magnitudes are ≈ 0.2 and ≈ 2.0 mag fainter in *W3* and *W4*, respectively, compared to the ALLWISE release (Wright et al. 2010). Extracting robust photometry might be difficult since the two stars are hardly resolved at *W4*. So, while there seems to be evidence for IR excess, the magnitude is yet to be determined. A more detailed analysis of the potential circumstellar disk will be deferred to a followup work.

The retrieved stellar parameters are provided in Table A. The error bars only represent the statistical uncertainties estimated with the Bayesian inference, so these might be underestimated as model-dependent systematics are not considered. The effective temperature, $T_{\text{eff}} \approx 9540$ K, is consistent with an A0V type star as evolutionary tracks predict about 9500 K for a stellar mass of $M_* = 2.2 M_\odot$ (see Fig. A.2). The posterior of the metallicity peaks towards zero, which is the lower boundary of the model grid, so favoring solar abundances. The visual extinction, $A_V \approx 0.2$, is consistent with the value derived for HD 135344 B, $A_V = 0.23 \pm 0.06$, by Fairlamb et al. (2015). The radius, $R_* \approx 1.5 R_\odot$, is smaller than model predictions, $R_* = 1.8 R_\odot$. The radius acts as a flux scaling of the model spectrum, together with the normal prior for the parallax. The Gaia astrometric solution has a RUWE of 0.95 and the astrometric excess noise is 0.21 mas, so the parallax measurement seems sufficiently accurate to not bias the inferred stellar radius. From T_{eff} and R_* , we computed a bolometric luminosity of $\log L_*/L_\odot = 1.22 \pm 0.01$. The luminosity is low for an A0V type star (see Fig. A.2), as a result of the small stellar radius.

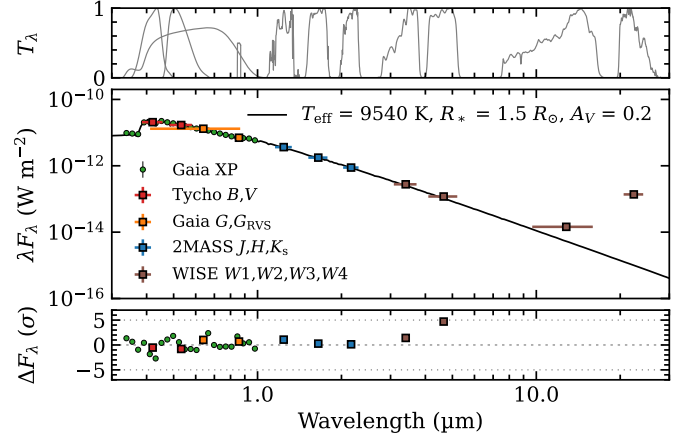


Fig. A.1: Spectral energy distribution of HD 135344 A. The black line is the best-fit model spectrum and the colored markers are the photometric fluxes with horizontal error bars showing the full width at half maximum of the filters. The top panel shows the filter profiles and the bottom panel the residuals relative to the measurement uncertainties. For clarity, every 15th wavelength of the Gaia XP spectrum is shown, whereas the full spectrum was used in the fit.

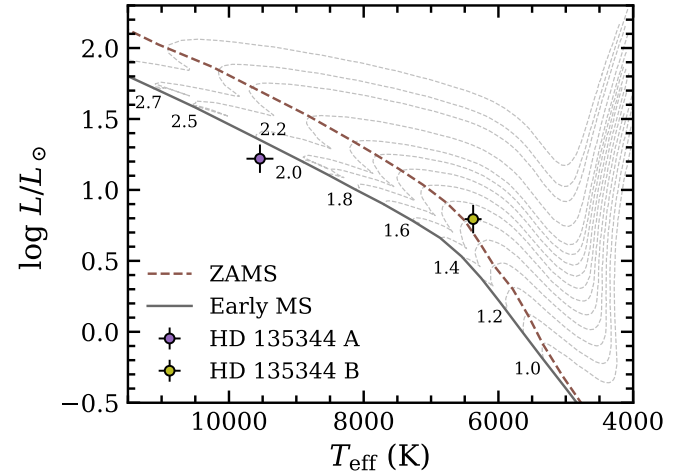


Fig. A.2: Stellar evolutionary tracks in comparison with the HD 135344 AB binary system. The parameters of the primary star have been estimated in this work, but here with inflated uncertainties of $\sigma_{T_{\text{eff}}} = 200$ K and $\sigma_{\log L/L_\odot} = 0.1$ dex. The parameters of the secondary star have been adopted from Fairlamb et al. (2015) (corrected to the Gaia DR3 distance), and the pre-main-sequence tracks are from Siess et al. (2000). Stellar masses are given in solar masses next to the pre-main-sequence tracks. The brown dashed line shows the zero age main-sequence (ZAMS; $L_{\text{nuclear}} > 0.99 L_{\text{total}}$), which is at 13.7 Myr for HD 135344 B ($M_* = 1.5 M_\odot$), and the solid line is the early main-sequence (MS), defined as the moment when the CNO cycle of intermediate-mass stars has reached its equilibrium.

Table A.1: Stellar parameters of HD 135344 A.

| Parameter | Value | Units | Reference |
|------------------------------|---------------------|----------------------|--|
| RA (J2016) | +15 15 48.92 | hms | Gaia Collaboration et al. (2023) |
| Dec (J2016) | -37 08 56.12 | dms | Gaia Collaboration et al. (2023) |
| μ_{RA} | -18.74 ± 0.05 | mas yr ⁻¹ | Gaia Collaboration et al. (2023) |
| μ_{Dec} | -24.01 ± 0.04 | mas yr ⁻¹ | Gaia Collaboration et al. (2023) |
| ϖ | 7.41 ± 0.04 | mas | Gaia Collaboration et al. (2023) |
| TYCHO <i>B</i> | 7.861 ± 0.015 | mag | Høg et al. (2000) |
| TYCHO <i>V</i> | 7.775 ± 0.011 | mag | Høg et al. (2000) |
| Gaia <i>G</i> | 7.7481 ± 0.0028 | mag | Gaia Collaboration et al. (2023) |
| Gaia <i>G</i> _{BP} | 7.7687 ± 0.0028 | mag | Gaia Collaboration et al. (2023) |
| Gaia <i>G</i> _{RP} | 7.6794 ± 0.0038 | mag | Gaia Collaboration et al. (2023) |
| Gaia <i>G</i> _{RVS} | 7.6387 ± 0.0051 | mag | Gaia Collaboration et al. (2023) |
| 2MASS <i>J</i> | 7.582 ± 0.019 | mag | Cutri et al. (2003) |
| 2MASS <i>H</i> | 7.582 ± 0.036 | mag | Cutri et al. (2003) |
| 2MASS <i>K</i> _s | 7.563 ± 0.023 | mag | Cutri et al. (2003) |
| WISE <i>W</i> 1 | 7.538 ± 0.028 | mag | Wright et al. (2010) |
| WISE <i>W</i> 2 | 7.583 ± 0.022 | mag | Wright et al. (2010) |
| WISE <i>W</i> 3 | 7.140 ± 0.017 | mag | Wright et al. (2010) |
| WISE <i>W</i> 4 | 4.210 ± 0.019 | mag | Wright et al. (2010) |
| SPHERE <i>H</i> 2 | 7.59 ± 0.03 | mag | This work |
| SPHERE <i>H</i> 3 | 7.58 ± 0.03 | mag | This work |
| SPHERE <i>K</i> 1 | 7.57 ± 0.02 | mag | This work |
| SPHERE <i>K</i> 2 | 7.56 ± 0.02 | mag | This work |
| SpT | A0V | | Houk (1982) |
| T_{eff} | 9540 ± 100 | K | This work |
| log <i>g</i> | 4.1 ± 0.1 | dex | This work |
| [M/H] | $\lesssim 0.05$ | dex | This work |
| R_* | 1.50 ± 0.01 | R_{\odot} | This work |
| A_V | 0.21 ± 0.02 | mag | This work |
| log L/L_{\odot} | 1.22 ± 0.01 | dex | This work |